Slot-Die Deposition of CuSCN Using Asymmetric Alkyl Sulfides as Cosolvent for Low-Cost and Fully Scalable Perovskite Solar Cell Fabrication

Iwan Zimmermann, Nao Harada, Thomas Guillemot, Celia Aider, Kunnummal Mangott Muhammed Salim, Van Son Nguyen, Jean Castillon, Marion Provost, Karim Medjoubi, Stefania Cacovich, et al.

Slot-Die-Deposition of CuSCN Using Asymmetric Alkyl Sulfides as Co-Solvent for Low-Cost and Fully Scalable Perovskite Solar Cell Fabrication

Iwan Zimmermann, Nao Harada, Thomas Guillemot, Celia Aider, K. M. Muhammed Salim, Van Son Nguyen, Jean Castillon, Marion Provost, Karim Medjoubi, Stefania Cacovich, Daniel Ory, Jean Rousset*

I. Zimmermann, N. Harada, T. Guillemot, K. M. M. Salim, V. S. Nguyen, J. Castillon, M. Provost, K. Medjoubi
Institut Photovoltaïque d'Île-de-France (IPVF), 18 Boulevard Thomas Gobert, Palaiseau, 91120, France
E-mail: iwan.zimmermann@ipvf.fr

S. Cacovich
Institut Photovoltaïque d'Île-de-France (IPVF), UMR 9006, CNRS, Ecole Polytechnique, IP Paris, Chimie Paristech, PSL, Palaiseau, 91120, France

C. Aider, D. Ory, J. Rousset
Institut Photovoltaïque d'Île-de-France (IPVF), 18 Boulevard Thomas Gobert, Palaiseau, 91120, France
EDF R&D, 7 Boulevard Gaspard Monge, 91120 Palaiseau, France

Keywords: photovoltaics, perovskites, upscaling, CuSCN, slot-die coating, multidimensional imaging

The development of industrially relevant deposition processes for efficient, stable, and inexpensive charge extracting layers is crucial for the commercialization of perovskite solar cells (PSC). This work demonstrates, for the first time, the deposition of copper thiocyanate (CuSCN) as a low-cost and reliable hole transport layer using slot-die-coating. Methyl ethyl sulfide (MES) is thereby used as an asymmetric co-solvent to significantly increase the solubility of CuSCN in the utilized slot-die ink compared to traditional pure diethyl sulfide (DES) based solutions. Optimized CuSCN inks allow for the deposition of CuSCN layers on 5 x 10 cm^2 substrates with a wide range of thicknesses. Multidimensional imaging photoluminescence techniques are used to investigate the uniformity of the CuSCN thin films deposition as well as the influence of the solvent on charge losses. Finally, the CuSCN slot-

die deposition is integrated into a fully up-scalable PSC fabrication process showing 19.1% power conversion efficiency for small laboratory cells and 14.7 % for 9 cm^2 mini-modules. Furthermore, semi-transparent mini modules retained 80% of their initial efficiency after 500h of constant illumination.

1. Introduction

Halide perovskites have attracted great attention over the last few years for their use as efficient light absorber materials in thin film solar cells.[1] Single junction perovskite solar cells (PSC) already reached power conversion efficiencies above 26% under laboratory conditions.[2] The capability of fabricating PSCs from cheap solution-based processing methods as well as their potential use in perovskite/silicon tandem solar cells has attracted considerable commercial interest in this technology.[3,4] However, important questions such as the long-term stability of PSCs as well as the scale-up of the PSCs to an industrial production level remain major bottlenecks. Various industrially compatible wet deposition techniques were investigated to deposit uniform perovskite thin films at a large scale. This includes slot-die coating,[5,6] blade-coating,[7–9] spray coating,[10] or ink-jet printing.[11] To tackle stability as well as scalability of PSCs not only the perovskite material itself has to be addressed, but also its adjunct charge extracting layers, namely the electron transport layer (ETL) and the hole transport material (HTM). In an n-i-p configuration titanium oxide and tin oxide are well established ETLs demonstrating both high efficiencies and stability at moderate materials cost. Chemical bath deposition, atomic layer deposition (ALD), slot-die-coating, screen printing as well as spray deposition have been employed for uniform deposition of these n-type oxides at the large scale. For the p-type extraction layer an overwhelming number of organic small molecules and polymers have been proposed as HTMs in PSCs.[12,13] The most common ones used in literature today are spiro-OMeTAD and PTAA. Due to the low intrinsic conductivity of such organic HTMs, dopants must be added to achieve good device efficiencies. However, dopants were shown to be a source of instability within PSCs.[14] Moreover, organic HTMs are expensive, limiting their practical use at the industrial level. Consequently, research efforts are being deployed to find simple, cheap inorganic HTMs that can be used in their pristine form without the need of including dopants. Promising inorganic HTMs found in the literature include NiOx,[15–17] $CuGaO_2$,[18] CuSCN[19–25] or CuI.[26–28] Solution processing of inorganic HTMs can be difficult as e.g. oxides require high annealing temperatures not compatible with the perovskite material. Oxide materials are therefore commonly employed in an inverted solar cell configuration. For the p-i-n device polarity,

NiO_x quickly emerged as one of the most promising inorganic HTM with PCEs surpassing 23%[15].

On the other hand, for solution processible deposition of an inorganic HTM on top of perovskite, CuSCN has been shown to be a highly promising candidate, with power conversion efficiencies exceeding 20% being reported.[20,24,25] CuSCN is a large band gap material with a high transparency in the UV-Vis and NIR spectral region which also makes it suitable for perovskite/silicon tandem applications. Furthermore, CuSCN has an ideal energy band alignment with the perovskite for hole extraction, and a high intrinsic hole mobility and conductivity.[29] Despite its excellent properties as hole extracting material and good performances demonstrated in previous studies, relatively few publications on the use of CuSCN in PSCs can be found in the literature. This can most likely be attributed to the low solubility of CuSCN in generally used alkyl sulfides complicating the growth of well covering films with a desirable thickness. Furthermore, it has been reported that thioethers can damage the perovskite layer. Buffer layers are therefore commonly used to protect the HTM/perovskite interface during deposition.[30] Spin-coating is the most used technique to grow CuSCN thin films. Alternative deposition methods such as doctor blading have been investigated to gain more control on the layer thickness.[31] On the other hand aerosol chemical vapor deposition has been used to grow dense 1.5µm thick CuSCN layers using a heated reactor chamber[32]. Furthermore, a smart-bottle humidifier-assisted deposition of CuSCN mist directly on the perovskite films displayed a PCE of 18.8%[33].

In this work, we demonstrate the deposition of CuSCN using slot-die coating. We show that the use of methyl ethyl sulfide (MES) as an asymmetric solvent leads to an increased solubility of the CuSCN material compared to pure ethyl sulfide (ES) based solutions. This allows the deposition of CuSCN films with a wide range in thickness by varying the coating speed. Eventually, homogeneous coating of CuSCN on perovskite films with an optimal layer thickness of around 100 nm were achieved. Small devices and mini-modules in nip configuration were fabricated using a fully up-scalable fabrication process combining the chemical bath deposition of SnO_2 n-type extraction layer and the slot die coating of both the perovskite absorber layer and the top CuSCN p type extraction layer. Efficiencies up to 19.1% for small cells and 14.7% for 9 cm^2 mini-modules were obtained with this industrially relevant fabrication process. Moreover, semi-transparent mini-modules retained more than 80% of their initial efficiency after 500h of continuous illumination.

2. Results and Discussion

2.1. Fully up-scalable device architecture

A schematic drawing of the perovskite solar cell fabrication process is shown in **Figure 1a**.

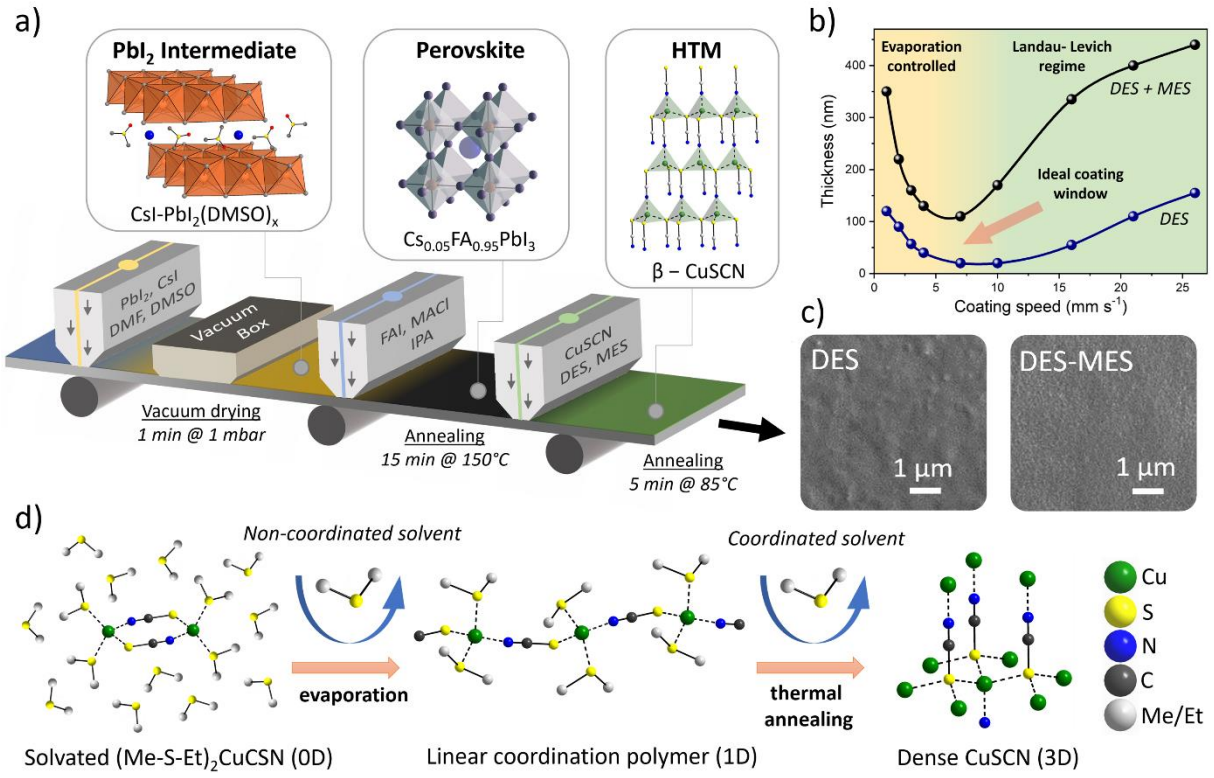

Figure 1. CuSCN deposition process and formation mechanism: (a) Schematic representation of the deposition process by slot-die coating. Sequential deposition of double cation perovskite followed by slot-die coating of CuSCN on top of the perovskite layer. (b) Layer thickness of the slot-die coated CuSCN related to the coating speed. The film thickness is greatly influenced by the coating speed. Using MES as a co-solvent allows for CuSCN inks with increased concentrations leading to thicker CuSCN layers. (c) SEM top-view images of the CuSCN film on perovskite. CuSCN films deposited from DES are not thick enough to fully cover the perovskite layer. On the other hand, with MES as a co-solvent uniform coverage of the perovskite can be achieved. (d) CuSCN layer formation mechanism: Solvated CuSCN forms an intermediate coordination polymer after evaporation of non-coordinated solvent, which then further transforms into dense CuSCN after thermal annealing.

For this work we target a fully scalable device stack using industrially compatible deposition techniques and low-cost materials. The n-i-p cell architecture used in this work consists of tin oxide deposited by chemical bath deposition (CBD), sequentially slot-die coated double cation perovskite and slot-die processed CuSCN. The slot-die deposition process is schematically illustrated in Figure 1a. The low temperature CBD process previously developed in our lab was used to deposit a uniform layer of SnO_2 onto the FTO substrates.[34] The average thickness of SnO_2 is around 25nm, which is achieved by two CBD runs to ensure pinhole-free coverage of the FTO surface. Although CBD is a relatively slow deposition process it can be considered scalable by running a highly parallelized batch fabrication to

ensure a sufficient sample production throughput. For the perovskite we use a two-step slot-die deposition method.[35] Perovskite deposition is performed under inert atmosphere to prevent degradation. Compared to previous reports we implemented the simpler MA-free composition $Cs_{0.05}Fa_{0.95}PbI_3$ for improved stability and better efficiency. Furthermore, we used MACl as an additive for better crystallization control and increased grain size. The XRD pattern and SEM pictures of the obtained perovskite films can be found in Figure S1. SEM cross-sectional images reveal a well crystallized perovskite film with a thickness of around 500 nm. A small amount of unreacted PbI_2 visible in XRD is very common in sequentially deposited perovskite, contributing to grain passivation.[36] Finally, the CuSCN is slot-die coated onto the perovskite under ambient atmosphere using alkyl sulfide-based inks. The as coated film is then further annealed at 85°C for 5min to form a dense film of CuSCN. Devices are finalized by either evaporating gold for opaque solar cells or sputtering of ITO for semi-transparent samples. We note that even though the main layers in the solar cell stack are deposited by up-scalable deposition methods, passivation layers that are added between the absorber and the extraction contact are deposited by spin-coating. We use KCl on the SnO_2 as a surface treatment and PMMA on the perovskite as a thin interlayer to achieve best efficiencies as well as to suppress hysteresis.

2.2 CuSCN ink design and slot-die coating

CuSCN is deposited onto the perovskite layer by slot-die coating using various thioether-based inks. Selecting solvents with a high solubility for CuSCN that are not dissolving or harming the perovskite film is challenging. The most common solvent used for the deposition onto perovskite found in the literature is diethyl sulfide (DES). The solubility of CuSCN in DES lies in the range of 30-40 mg/ml while highly concentrated solutions tend to form precipitates. For the slot-die experiments a concentration of 30mg/ml was utilized to avoid precipitation of CuSCN in the experimental setup. To further improve its solubility, methyl ethyl sulfide (MES) was used as a co-solvent to achieve more concentrated inks. MES was found to have a much better solubility (>250 mg/ml) than DES but is also more aggressive to the perovskite. In fact, we found that the perovskite bulk is relatively stable when dipping the samples into the sulfide solvents for several minutes. However, we observe degradation on the perovskite surface with MES which is shown in Figure S2. This interface degradation can be followed by an increase in absorption. To minimize degradation of the perovskite layer 3:1 (v:v) mixtures of DES and MES (from here on labeled as DES-MES) were used with a CuSCN concentration of 70 mg/ml to form the ink. The CuSCN was slot-die coated onto the

perovskite layer previously passivated with a thin PMMA layer. Initially, the slot-die deposition was optimized by changing the speed of the slot-die head during the deposition. Simultaneously, the ink dispense rate was adjusted to obtain the best possible film uniformity at a given coating speed. As a first approximation, the dispense rate was adjusted linearly to the coating speed. **Figure 1b** displays the thickness of CuSCN layers fabricated at different coating speeds deducted from SEM cross-section images. The cross-section images are presented in supplementary Figure S3. The slot-die coating can be divided into two regimes: (a) evaporation-controlled regime with an increased film thickness at low coating speeds and (b) Landau-Levich regime with thicker CuSCN layers towards higher coating speeds. The ideal coating condition, resulting in the most uniform film, typically lies in between the two regimes with the lowest film thickness. At very low coating speeds the deposition of the wet film is driven by evaporation-controlled phenomena. The evaporation of solvent from the meniscus during the coating leads to chatter along the coating direction with a very irregular film formation. This is often referred to as the "coffee ring effect"[37,38] with the formation of an oscillating thickness gradient in the film. This coating defect can be clearly seen on samples coated with 1mm/s (Figure S3). On the other hand, at fast coating speeds the film is dragged out by viscous forces. Thereby the evaporation during the coating can be neglected and the drying occurs afterwards. Due to the fast movement speed of the slot-die the meniscus does not have enough time to stabilize and therefore the coating becomes irregular at fast speeds. Furthermore, film defects might occur from air entrainment into the meniscus caused by the fast-moving slot-die head. Moreover, thick layers are no longer shiny due to the increased surface roughness (Figure S3). Although with DES based inks the CuSCN thickness could be varied between around 20-150 nm, the thicker films were of poor quality due to the extreme coating conditions needed. However, with the DES-MES ink the CuSCN thickness could be significantly improved without compromising the film uniformity. Thicker CuSCN layers also significantly improve the surface coverage as shown from top view SEM images (**Figure 1c**). The ideal coating speed for the best film uniformity was 7 mm/s resulting in a CuSCN thickness of around 100 nm (Figure S4).

2.3 Thin film formation and morphology

Thioethers are soft Lewis bases that are well known solvents to coordinate and solubilize soft Lewis acid transition metal ions such as Cu^+ or Ag^+ salts.[39,40] The simplest coordination complex is thereby the formation of rhomboidal dimers with the formula $(R_2S)_2CuX$ (R=alkyl chain, X= I, Br, Cl, SCN).[41] By dissolving CuSCN into a DES-MES solvent mixture we

expect therefore the formation of (Me-S-Et)$_2$CuSCN (Me=CH_3, Et=CH_2CH_3) complexes within the ink solution. A schematic example of solubilized CuSCN in the form of dimers is shown in **Figure 1d**. Thereby the MES ligands coordinate the copper ions due to their higher coordination strength compared to DES which acts as the diluting solvent. Due to the low boiling point of alkyl sulfides, non-coordinated solvent molecules are quickly removed by evaporation after the slot-die deposition leaving behind an intermediate film in the form of a linear coordination polymer. This kind of linear coordination polymer was found to exist for both dimethyl sulfide and DES when crystallized with CuSCN.[42] We therefore assume that a similar coordination polymer is also present in our case with MES. These intermediate coordination polymers are relatively unstable as the coordinated thioether solvent molecules are gradually released from the structure. This process is accelerated by placing the samples on a hotplate to remove the coordinated solvent by thermal annealing. This will break up the linear coordination polymer and dense layers of CuSCN remain. This transition was further confirmed by XRD diffraction experiments from drop-cast CuSCN layers onto glass substrates (Figure S5). The presence of diffraction peaks of the CuSCN intermediate phase can be observed on the non-annealed sample and completely vanish upon heating the sample to 85°C for 10 min, while the typical diffraction peaks of β-CuSCN appear.[43] We note that the fabrication of a thick CuSCN layer by drop-casting was necessary to obtain sufficient signal from the XRD analysis. For the slot-die coated samples, the final CuSCN crystallites formed during this process are very small as can be observed by the SEM surface images in Figure 1c. This is further confirmed by XRD diffraction experiments where we could not observe any diffraction peaks from the CuSCN phase, indicating that the films are close to amorphous. This is in line with previous studies where synchrotron radiation was needed to resolve the diffraction peaks of the beta-CuSCN film.[20] With DES-based inks, the coverage of the perovskite layer is not complete. From the SEM images (Figure 1c) we can partially see the underlaying grain structure of the perovskite. On the other hand, DES-MES-based inks can fully cover the roughness of the perovskite layer resulting in a much smoother surface morphology.

2.4 Optical characterization

The uniformity and optoelectronic properties of slot-die coated CuSCN films were studied by wide-field hyperspectral photoluminescence (PL) imaging (HI).[44,45] In addition, time-resolved photoluminescence (TRPL) experiments were performed to probe charge carrier dynamics. Specifically, we compare two distinct solvent conditions for the CuSCN

deposition: DES and DES-MES, as shown in **Figure 2**. The sample stacks adhere to the following architecture: Glass/FTO/SnO_2/Perovskite/PMMA/CuSCN.

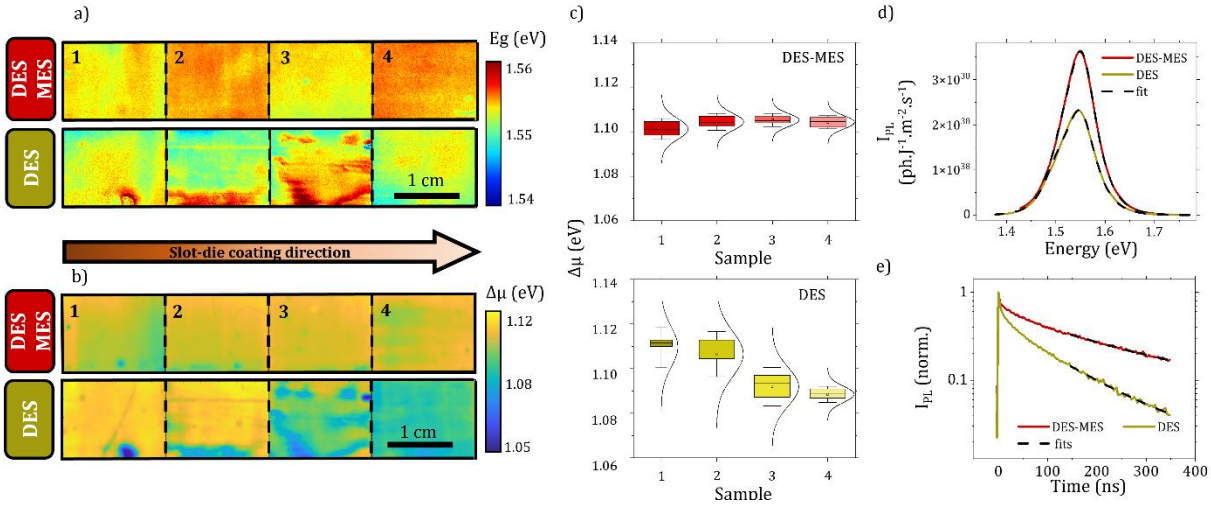

Figure 2 Optical characterization of samples with slot-die deposited CuSCN using two different solvent conditions: DES-MES and DES. Wide-field hyperspectral photoluminescence maps: (a) Band gap maps and (b) Quasi-fermi level splitting maps. All 4 samples of a respective solvent condition were measured together in the hyperspectral setup. The slot-die deposition process started from sample n°1 and ended at sample n°4.
(c) Samples' QFLS distributions with average values and standard deviations as a function of the sample. (d) Average PL spectra of samples n°4 for the DES-MES and DES solvent condition. The dotted lines are the fit to the data using a Boltzmann distribution.
(e) Normalized time resolved photoluminescence (TRPL). The dotted lines are the fit to the data using a mono-exponential decay between 100 ns and 300 ns.

The samples with CuSCN deposited by slot-die on 5x10 cm² substrates were cut in four parts along the coating direction. Large-scale absolutely calibrated photoluminescence (PL) spectra images[46] were acquired using blue LEDs (405nm) at 96.4 mW/cm² (0.83 sun) power illumination with the samples excited from the thin film side. The calibrated spectra were then fitted using a model based on Planck's law (**Equation 1**).[47,48]

$$I_{PL}(E) = \frac{2\pi E^2 a(E)}{h^3 c^2 \exp\left(\frac{E-QFLS}{kT}\right)-1} \quad (1)$$

E represents the photon energy, a(E) the absorptivity of the absorber, *h* the Planck constant, *c* the speed of light, *k* the Boltzmann constant, QFLS the quasi-Fermi level splitting, and T the temperature. All QFLS values are post-corrected to match 1 sun equivalent illumination. Additional details on the temperature and Urbach energy fits are illustrated in Figure S6.

We thus fit the PL spectra pixel by pixel, obtaining the bandgap energy (Eg) and quasi-Fermi levels splitting (QFLS) maps, reported in **Figure 2a** and **Figure 2b**. As an example, the PL

average spectra and their respective fits for sample n° 4 for the DES and DES-MES solvent conditions are depicted in **Figure 2d**. The fitted bandgaps of the perovskite on the two samples are comparable and in the range of 1.54 to 1.56 eV, i.e between 797 and 804 nm and remain constant in average along the slot-die deposition process (Figure 2a). The dispersion (standard deviation) for the CuSCN (DES-MES) samples is less than 0.5 meV, whereas the CuSCN (DES) samples exhibit dispersion values around 1 meV. Nevertheless, these low dispersion values indicate a nearly constant bandgap value. This observation suggests that the use of the two solvents did not cause any chemical change to the perovskite composition. Indeed, the formation of new chemical phases would typically be indicated by the emergence of an additional PL peak or a shift of the PL peak[49]. Moreover, the CuSCN (DES-MES) sample shows an average QFLS of 1.10 eV, as well as the smallest standard deviation of 4 meV in **Figure 2c** (see Table S1 for more details). CuSCN (DES) has a slightly lower QFLS of 1.09 eV but with a higher dispersion around 10 meV. The level of homogeneity of the QFLS maps were then evaluated in Figure 2c. For CuSCN (DES) samples the QFLS shows a much larger variation compared to the CuSCN deposited with a DES-MES solvent mixture. This further confirms a non-conformal coverage of the perovskite layer by CuSCN using DES based inks. Finally, to have an insight of the carrier recombination dynamics, TRPL measurements, under a fluence of $5 \cdot 10^9$ ph/cm²/pulse, were performed on all the samples label n°2 over an area of 0.45 cm². The results are shown in **Figure 2e**. The experimental curves were fitted using a mono-exponential decay in the range of 100-350 ns. In this range, diffusion and radiative recombination become negligible compared to non-radiative (SRH) bulk, HTL-top-surface, and ETL-SnO_2-bottom-surface ones. CuSCN (DES-MES) shows the highest carrier lifetime value with 200 ns compared to DES with 125 ns. This value traduces the minority-charge-carrier lifetime and is directly related to the charge recombination rate in the sample [50–52], which confirms the steady state PL measurements as previously discussed. To avoid any chemical reaction of the sulfide based solutions with the perovskite, we utilized PMMA as a thin protective layer on top of the perovskite film as previously demonstrated by Xu et al [30]. The efficiency of PMMA as a protective layer is illustrated in Figure S7. Without the PMMA layer, a significative decrease of PL intensity is observed together with strong PL inhomogeneities over the samples' position. The same trend could be observed from TRPL measurements where the presence of PMMA improved the charge carrier lifetime to 150 ns compared to 85 ns without PMMA. To summarize the optical characterization, the use of HI PL identified a single-phase composition regardless of the solvent condition, but the use of DES solvent alone introduced a decrease in QFLS along the slot die direction.

2.5 Devices and mini-modules

CuSCN layers fabricated from DES and DES-MES based inks were integrated in full devices, in an n-i-p configuration (**Figure 3a**). As a control condition spiro-OMeTAD was used as the reference HTL deposited by spin-coating. The results of the small area (active area: 0.09 cm^2) devices are summarized in **Figure 3b** and the corresponding photovoltaic parameters are listed in **Table1**.

Small devices (0.09 cm^2)	**V_{OC} [V]**	**J_{SC} [mA cm^{-2}]**	**FF [%]**	**PCE [%]**
CuSCN (DES) (FW / RV)	0.99 / 0.98	21.1 / 21.0	68.2 / 67.0	14.2 / 13.8
CuSCN (DES-MES) (FW / RV)	1.08 / 1.10	23.5 / 23.5	76.0 / 73.9	19.3 / 19.1
Spiro-OMeTAD (FW / RV)	1.13 / 1.13	23.9 / 23.9	75.7 / 74.2	20.4 / 20.0
Mini-modules (9 cm^2)	**V_{OC} [V]**	**J_{SC} [mA cm^{-2}]**	**FF [%]**	**PCE [%]**
CuSCN (DES-MES) (FW / RV)	6.09 / 6.09	3.70 / 3.65	64.4 / 66.1	14.5 / 14.7
Spiro-OMeTAD (FW / RV)	6.38 / 6.39	3.74 / 3.75	70.2 / 69.3	16.8 / 16.6
Semi-transparent (9.6 cm^2)	**V_{OC} [V]**	**J_{SC} [mA cm^{-2}]**	**FF [%]**	**PCE [%]**
CuSCN (DES-MES) (FW / RV)	8.14 / 8.12	2.68 / 2.66	59.1 / 60.6	12.9 / 13.1
PTAA (FW / RV)	8.76 / 8.71	2.77 / 2.78	60.9 / 61.0	14.8 / 14.8

Table 1 Summary of photovoltaic parameters of devices and mini-modules.

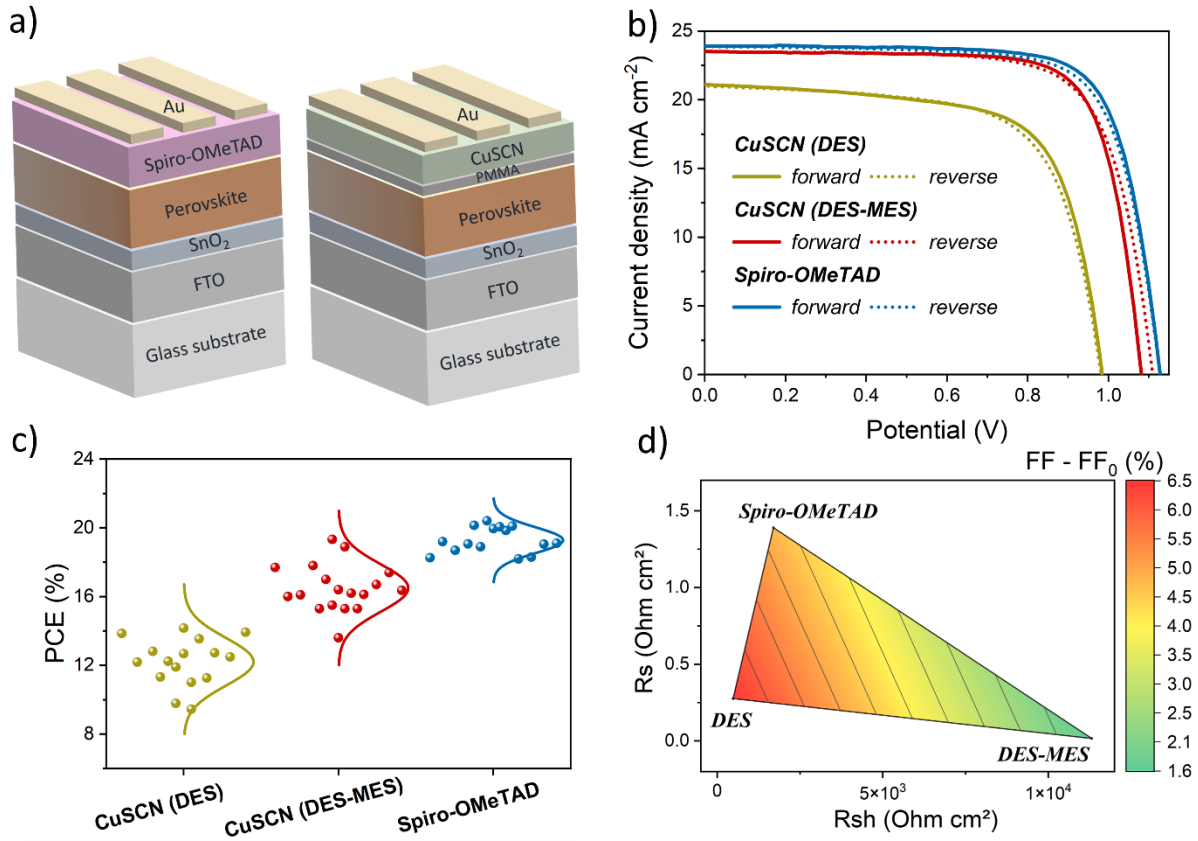

Figure 3. Photovoltaic performance of small area devices. (a) Schematic drawing of the device architectures. (b) IV-curves of champion devices fabricated from CuSCN deposited by DES and DES-MES based inks and Spiro-OMeTAD as reference. (c) device statistics for 16 devices for each condition. (d) Fill Factor loss " FF_0 -FF" for averaged data by composition, plotted as a function of R_{sh} and R_s.

Figure 3a shows the current voltage (J-V) curves of the champion devices for each condition. The CuSCN (DES-MES) reference device exhibits the lowest power conversion efficiency, approximately measuring 14%. The low device efficiency mainly arises due to a lower V_{OC} and J_{SC} compared to the Spiro-OMeTAD control sample. This observation is consistent with the morphological and optical characterizations of thin CuSCN layers obtained using pure DES as the solvent. Incomplete coverage of the perovskite layer by CuSCN may result in direct contact of the gold electrode with the perovskite absorber explaining the low shunt resistance observed in such devices. Furthermore, as shown above, such a poor interface leads to non-radiative recombination responsible for a V_{OC} lower than 1V. On the other hand, devices with CuSCN deposited from DES-ME inks display a significantly improved performance with efficiencies > 19%. The V_{OC} and J_{SC} of the CuSCN champion device are at 1.1 V and 23.5 $mAcm^{-2}$ respectively in reverse bias direction, comparable with the Spiro-OMeTAD reference cell (1.13 V, 23.9 $mAcm^{-2}$). Stabilized efficiencies are shown in Figure

S8. When comparing the optical QFLS with the electrical Voc [53], we only find a drop of 10 meV between the QFLS of DES-MES and DES, whereas the Voc has dropped by 100 meV. This significant difference between the drops in QFLS and Voc could be explained by the nature of the samples analyzed: for the electrical measurements, an additional layer of gold electrode was deposited, whereas this layer was absent for the optical measurements. As mentioned above, the incomplete coverage of the CuSCN using DES solvent might result in a direct contact between the gold electrode and the perovskite resulting in a reduction of the electrical properties. The J_{SC} was further confirmed by performing external quantum efficiency measurements (EQE) shown in Figure S8 and the values were found to closely match the ones obtained from the J-V curves. **Figure 3d** shows the efficiency distribution over 16 devices from each category. For CuSCN samples we observe a slightly wider efficiency distribution compared to the Spiro-OMeTAD references. This may arise from a slightly less uniform CuSCN layer compared to Spiro-OMeTAD.

To explain further the performance losses of CuSCN compared to Spiro-OMeTAD, we fitted the light (J-V) curves for all cells with a single diode model. For the devices terminated by a Spiro-OMeTAD HTL the ideality factor is remarkably close to n=2, the theoretical value for an intrinsic semiconductor. However, ideality factors are significantly increased (ranging from 3.5 to 4.7) for devices with CuSCN deposited from DES and DES-MES based inks. According to the work from M. Green,[54] a normalized V_{oc} is defined as $v_{oc} = \frac{qV_{oc}}{nkT}$ and helps comparing cells with different ideality factors "*n*". The Fill Factor free from parasitic resistances has been shown to be well approximated by the following expression $FF_0 = \frac{v_{oc} - \ln(v_{oc}+0.72)}{v_{oc}+1}$. A a high ideality factor leads to a drop of a FF_0 in the absence of series or shunt resistance (Figure S9). In average, absolute losses in FF_0, compared to the cell terminated with SpiroOMeTAD of 11.85% and 9.1% are measured for cells with CuSCN deposited from DES and DES-MES inks respectively. In addition, in Figure 3d the gap between the experimental FF and FF_0-FF, that can be directly related to the impact of parasitic resistive losses, is plotted as a function of shunt and series resistance, (see more detailed statistics in Figure S10). The additional Fill Factor loss due to resistances is on average about 6.5% and 1.6 % for samples terminated by CuSCN (DES) and CuSCN (DES-MES) to be compared 4.8% for Spiro-OMeTAD terminated ones. This is well explained by the resistance differences measured with different types of HTL layers. For example, the CuSCN (DES-MES) terminated devices present the lowest FF-FF_0 drop with the highest shunt resistances and the lowest series ones. We conclude that the increase of the ideality factor is the source of

performance decrease for CuSCN terminated devices compared to the ones with Spiro-OMeTAD. This drop is partially compensated for by the very low resistive loss in the case of CuSCN (DES-MES). However, the origin of very high values of ideality factors is not straightforward. It has been proposed in the case of silicon-based PV device that it arises from non-linear shunts or edges defect densities.[55] It has also been shown to be linked to very high defect densities at interface for III-V devices.[56] To our knowledge, the behavior is not yet fully explained in perovskite devices, although some authors already described it in their work.[57]

To further investigate the deposition of CuSCN on larger substrates mini-modules with an aperture area of 9 cm^2 were fabricated using the optimized DES-MES based ink. Opaque modules consist of 6 cells in series with an area of 1.5 cm^2 per cell and a geometrical fill factor of around 93%. The reverse IV-curves of the champion modules are displayed in **Figure 4a**. CuSCN modules showed efficiencies up to 14.7 compared to 16.6% for the Spiro-OMeTAD reference. Like for the small devices the performance of the CuSCN-terminated modules is slightly lower. A PL intensity map of a CuSCN mini-module measured from the glass side is shown in **Figure 4b**. The map reveals the homogeneity of the module's PL intensity with the presence of the six distinct cells. The main loss is observed in the V_{OC} which could be an indication for slight non-uniformities in the CuSCN layer such as pinholes or thickness gradients. This coating defects might occur during the slot-die process involving highly volatile sulfide-based solvents. To our knowledge our work reports for the first time on CuSCN implemented in mini-modules. This is most likely due to the difficulties of fabricating uniform well-covering layers of CuSCN by spin-coating which highlights the importance of developing scalable deposition techniques.

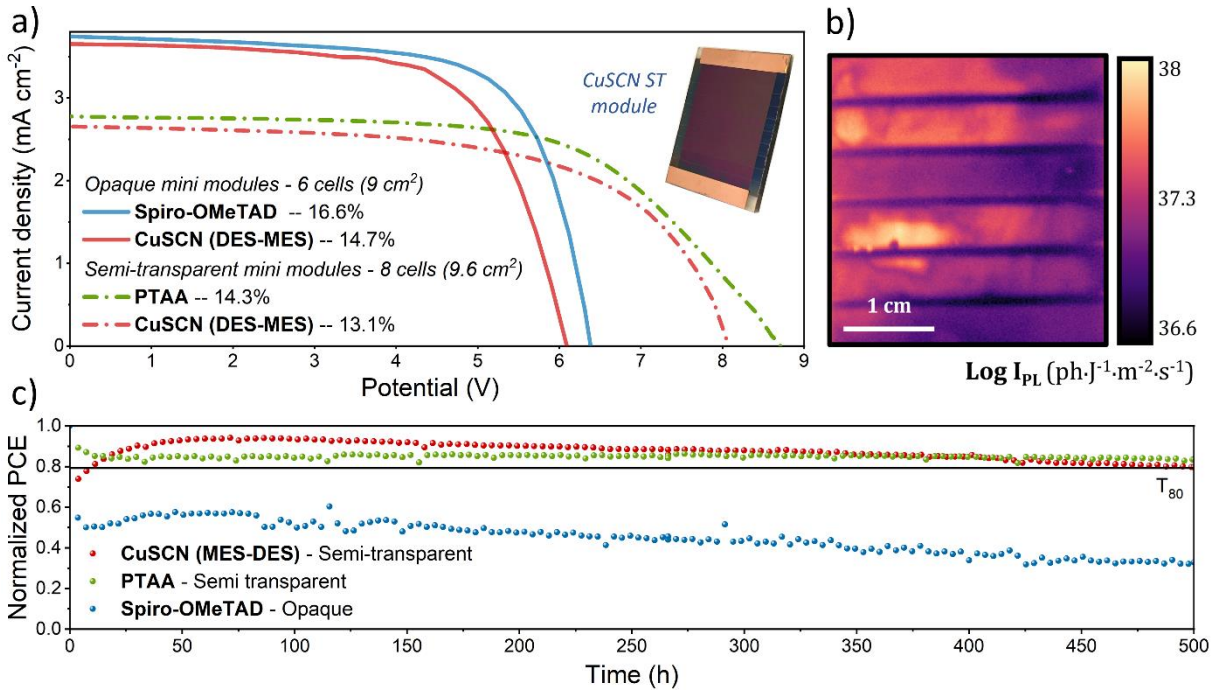

Figure 4. Photovoltaic performance of mini modules. (a) reverse J-V curves of opaque and semi-transparent mini-modules with CuSCN and Spiro-OMeTAD or PTAA as reference. (b) Photoluminescence mapping of an opaque CuSCN (DES-MES) mini-module centred at 800 nm. PL intensity is shown in log scale. (c) stability of the semi-transparent CuSCN and PTAA mini-modules compared to an opaque Spiro-OMeTAD based mini-module. Maximum power point tracking at 1 sun under nitrogen atmosphere.

2.5 Semi-transparent mini-modules and stability

Previous reports on CuSCN based devices show that the gold from the electrode can easily diffuse into the CuSCN layer leading to fast degradation.[20] This process seems to be accelerated under illumination as the CuSCN based devices were found to be relatively stable and can be stored in dark for several months without performance loss. For investigating the stability of the CuSCN based mini-modules under illumination the gold electrode was therefore replaced by a sputtered ITO top contact. To minimize losses from the low conductivity top TCO the cell pitch was reduced to 0.4mm increasing the number of cells connected in series to 8 with a module aperture area of 9.6 cm^2. Due to delamination problems of ITO on spiro-OMeTAD we decided to use PTAA instead for the control samples. The IV-curves of the semi-transparent mini-modules are displayed in Figure 4a. The PCE of semi-transparent CuSCN modules is 13.1% and the PTAA based mini module is at 14.3%. The slightly lower efficiencies compared to the opaque mini-modules originate on one hand from the incomplete absorption of the perovskite in the range from 600-800nm. The absence of the back reflection of the light by the gold layer leads to a lower short circuit current. An

optimization of the perovskite thickness would be necessary to optimize the efficiency of semi-transparent devices. On the other hand, higher resistance losses arising from the less conductive ITO result in a reduced fill factor in these mini-modules. Overall, the trend in semi-transparent samples is comparable to the opaque ones with CuSCN having slightly reduced Voc and Jsc compared to the control sample. The transmission data for the semi-transparent mini-modules is shown in Figure S11. Both mini modules show a high transparency in the near infrared region with around 78 % transmission at 900nm for the CuSCN mini-module. The high transmission makes this device stack very interesting for 4T tandem applications. We note that transparency could be further improved by applying an anti-reflective coating. For the stability measurement under light soaking conditions the modules were placed in a nitrogen fille chamber and kept at 25°C. The modules were kept at their maximum power point and an IV curve was recorded every 10 minutes. The LED light source was set to AM1.5G and the test was carried out following the ISOS-L protocol. Normalized stability of 3 modules is presented in **Figure 4c**. The opaque Spiro-OMeTAD module displays a very sharp initial decay, losing around half of its initial efficiency in just a few hours. Semi-transparent CuSCN and PTAA based mini-modules display significantly improved stability. Both modules retain more than 80% of their initial efficiency after 500h under continuous illumination. For the CuSCN sample we observe an initial drop of efficiency which is almost fully recovered during the first 100h of measurement. For the PTAA control sample we observe a slight decrease of efficiency within the first 10h before stabilization at around 85%. Overall, these results are very promising for a fully scalable semi-transparent device architecture based on CuSCN as HTL.

3. Conclusions

In summary we demonstrate the deposition of uniform CuSCN films onto perovskite using slot-die coating. The use of the asymmetric co-solvent methyl ethyl sulfide allowed for an increased CuSCN concentration in the slot-die ink and thus thicker well CuSCN layers. Furthermore, we show that the CuSCN thickness can be tuned over a wide range of thicknesses by varying the coating speed. Optimized CuSCN layers with a thickness of around 100 nm allow for good coverage of the perovskite layer. Small devices with efficiencies up to 19.1 % were fabricated, which was very close to the spin-coated Spiro-OMeTAD reference cells. Mini modules display efficiencies of up to 14.7%. Moreover, semi-transparent CuSCN based mini modules were shown to retain more than 80% of their initial efficiency after 500h of operation under illumination. We believe that this work provides a

valuable contribution towards upscaling perovskite solar cells with industrially compatible fabrication techniques using cheap and stable materials.

4. Experimental Section/Methods

Materials: All chemicals were used as received without further purification. Lead iodide (PbI_2) ethyl sulfide (DES) and methyl ethyl sulfide (MES) were purchased from TCI Europe. Formamidinium iodide (FAI), and tris(2-(1H-pyrazol-1-yl)-4-tert-butylpyridine)cobalt(III) tri[bis(trifluoromethane)sulfonimide (FK 209) were obtained from Greatcell Solar. Conductive fluorine doped tin oxide (FTO) coated glass (Tec C10X) was obtained from Nipon sheet glass. Bis(trifluoromethane) sulfonimide lithium salt (Li-TFSI), dimethyl sulfoxide (DMSO), dimethylformamide (DMF), chlorobenzene, tert-butylpyridine (Tbp), tin(II) chloride dihydrate >99.99%, urea, hydrochloric acid (for analysis, 36 %) and thioglycolic acid were bought from Merck. Spiro-OMeTAD and PTAA were obtained from Borun New Materials.

Devices / mini-modules fabrication: Devices and mini-modules were fabricated onto fluorine-doped tin oxide (FTO) coated glass substrates (TEC-C10X). The substrates were cut and cleaned sequentially with a 2% aqueous detergent solution (RBS T 230) and isopropanol in an ultrasonic bath for 20 minutes, respectively. SnO_2 layers are deposited by chemical bath deposition (CBD). The CBD solution was prepared by mixing urea (7.5g), HCl (7.5ml), $SnCl_2 \cdot 2H_2O$ (1.625g) and thioglycolic acid (150µl) in H_2O (600 ml). This solution was aged for 3 days in the fridge at 4°C prior to use. The solution is then further diluted 5:1 with water. The CBD took place at 70°C for 1h immersing the 5x10 cm^2 substrates in the solution. The substrates were washed with water and dried under N_2 flow at the end of the deposition. Two deposition cycles were performed utilizing a fresh CBD solution each time. Subsequentially, the SnO_2 layers were heated at 180 °C for 1h on the hotplate and UV-ozone treated after cooldown. A 0.1M solution of KCl was spin-coated on top of the SnO_2 layers at 3000rpm for 30s following another annealing step at 180 °C for 1h. All substrates were UV-ozone treated for 15 min prior to use. Perovskite coating was performed using a commercial slot die coater from nTact in a controlled nitrogen atmosphere with H_2O and O_2 levels below 10 ppm. Substrates with dimensions of 5 cm x 10 cm were used for all coatings and later cut to the desired device/module size. The perovskite was deposited by sequential layer deposition as reported previously.[34] In short, CsI/PbI_2 was slot die coated from a 0.95 M solution of PbI_2 containing 5 wt% CsI dissolved in a DMF:DMSO (9:1; v:v). The distance between slot die-

head and substrate was fixed to 65 µm and the coating speed was 7.5 mm/s with a dispense rate of 2.8 µl/s and a delay time of 8s. The freshly coated substrates were dried under vacuum (1 mbar) for 1 minute before being stored in a closed plastic container prior to conversion. The ammonium cations were slot die coated onto the PbI_2 layer from a solution of MACl (100 mg) and FAI (940 mg) dissolved in isopropanol (23 ml). The distance between slot die-head and substrate was fixed to 65 µm and the coating speed was 5 mm/s with a dispense rate of 3.8 µl/s with a waiting time of 10s. After the coating, the substrates were immediately transferred onto a hotplate and annealed at 150 °C for 15 minutes. CuSCN was deposited by slot-die coating under ambient atmosphere. CuSCN inks were formulated dissolving CuSCN powder in DES or MES/DES mixtures. The solution was allowed to stir for 1h before filtering it through a 0.25µm PTFE syringe filter. The CuSCN was slot-die coated on 5x10 cm^2 perovskite substrates with a coating gap of 120µm, a dispense rate of 4µl/s, speed of 7 mm/s and a delay time of 8 seconds. Finally, the sample was annealed for 5min at 85°C on a hotplate. Spiro-OMeTAD was dissolved in chlorobenzene (80 mg ml^{-1}) and spin-coated onto the perovskite layer at 4000 rpm. Tbp, Li-TFSI, FK 209 were added as additives: 330 mol% Tbp, 50 mol% Li-TFSI from a 1.8 M stock solution in acetonitrile and 6 mol% FK209 from a 0.25 M stock solution in acetonitrile. PTAA was dissolved in toluene (10 mg/ml) and 4µ of Tbp and 2.5µl Li-TFSI from a 1.8 M stock solution in acetonitrile were added as additives. The PTAA was spin-coated at 3000 rpm onto the perovskite. For the contact, a layer of 100 nm gold was thermally evaporated under high vacuum conditions using a shadow mask. For semi-transparent devices a layer of 200 nm ITO was directly sputtered onto the CuSCN/PTAA.

Laser scribing: Laser scribing of the perovskite modules was performed using an Innolas ILS LT laser system (INNOLAS) with the advantage of being extremely precise (laser spot diameter of 10 µm). This system is equipped with a green laser (532 nm) delivering monochromatic pulses of 10 ps at 400 kH. P1 scribing on FTO substrates was performed at the maximum laser power (16 W) to ensure electrical insulation. P2 and P3 were done using green laser with powers of 10.5 W and 0.5 W respectively.

Characterization: Solar cell efficiencies were evaluated under 1 sun (100mW cm^{-2}) simulated sunlight using an AAA solar simulator from Newport equipped with a Xenon lamp. The light intensity was calibrated using a certified KG5 filtered Si reference diode from Newport. Current voltage (IV) curves (scan speed: 20 mV s^{-1}) as well as stabilized efficiencies of perovskite solar cells were measured with an Arkeo measurement system from Cicci research. XRD patterns were recorded using an Empyrean diffractometer from Panalytical set up in

Bragg-Brentano geometry. SEM images were recorded on a Merlin electron microscope from Zeiss. Hyperspectral luminescence data were acquired using a PhotonEtc Grand-EOS setup.

Supporting Information

Supporting Information is available from the Wiley Online Library or from the author.

Acknowledgements

This project has been supported by the French Government in the frame of the program of investment for the future (Programme d'Investissement d'Avenir – ANR-IEED-002-01). We thank Valerie Daniau and Frederique Donsanti for the deposition of the ITO top electrodes and Nicolas Loones for the support on the slot-die equipment.

Conflict of Interest

The authors declare no conflict of interest.

Data Availability Statement

The data that support the findings of this study are available from the corresponding author upon reasonable request.

Received: ((will be filled in by the editorial staff))

Revised: ((will be filled in by the editorial staff))

Published online: ((will be filled in by the editorial staff))

References

[1] A. Kojima, K. Teshima, Y. Shirai, T. Miyasaka, *J. Am. Chem. Soc.* **2009**, *131*, 6050.

[2] NREL, *Best Research-Cell Efficiencies: https://www.nrel.gov/pv/assets/pdfs/best-research-cell-efficiencies.20200803.pdf (accessed: December 2023).*

[3] X. Y. Chin, D. Turkay, J. A. Steele, S. Tabean, S. Eswara, M. Mensi, P. Fiala, C. M. Wolff, A. Paracchino, K. Artuk, D. Jacobs, Q. Guesnay, F. Sahli, G. Andreatta, M. Boccard, Q. Jeangros, C. Ballif, *Science* **2023**, *381*, 59.

[4] H. Li, W. Zhang, *Chem. Rev.* **2020**, *120*, 9835.

[5] J. Li, J. Dagar, O. Shargaieva, M. A. Flatken, H. Köbler, M. Fenske, C. Schultz, B. Stegemann, J. Just, D. M. Többens, A. Abate, R. Munir, E. Unger, *Advanced Energy Materials* **2021**, *11*, 2003460.

[6] L. Gao, K. Huang, C. Long, F. Zeng, B. Liu, J. Yang, *Appl. Phys. A* **2020**, *126*, 452.

[7] M.-C. Tang, Y. Fan, D. Barrit, X. Chang, H. X. Dang, R. Li, K. Wang, D.-M. Smilgies, S. (Frank) Liu, S. D. Wolf, T. D. Anthopoulos, K. Zhao, A. Amassian, *J. Mater. Chem. A* **2020**, *8*, 1095.

[8] H. Hu, Z. Ren, P. W. K. Fong, M. Qin, D. Liu, D. Lei, X. Lu, G. Li, *Advanced Functional Materials* **2019**, *29*, 1900092.
[9] X. Chang, J. Fang, Y. Fan, T. Luo, H. Su, Y. Zhang, J. Lu, L. Tsetseris, T. D. Anthopoulos, S. (Frank) Liu, K. Zhao, *Advanced Materials* **2020**, *32*, 2001243.
[10] J. E. Bishop, C. D. Read, J. A. Smith, T. J. Routledge, D. G. Lidzey, *Scientific Reports* **2020**, *10*, 6610.
[11] F. Mathies, E. J. W. List-Kratochvil, E. L. Unger, *Energy Technology* **2020**, *8*, 1900991.
[12] J. B. Hoffman, D. D. Astridge, S. Y. Park, F. Zhang, M. Yang, D. T. Moore, S. P. Harvey, K. Zhu, A. Sellinger, *ACS Appl. Energy Mater.* **2022**, *5*, 8601.
[13] X. Sun, Z. Zhu, Z. Li, *Front. Optoelectron.* **2022**, *15*, 46.
[14] H. D. Pham, T. C.-J. Yang, S. M. Jain, G. J. Wilson, P. Sonar, *Advanced Energy Materials* **2020**, *10*, 1903326.
[15] C. Li, Y. Zhang, X. Zhang, P. Zhang, X. Yang, H. Chen, *Advanced Functional Materials* **2023**, *33*, 2214774.
[16] X. Yin, Y. Guo, H. Xie, W. Que, L. B. Kong, *Solar RRL* **2019**, *3*, 1900001.
[17] N. Phung, M. Verheijen, A. Todinova, K. Datta, M. Verhage, A. Al-Ashouri, H. Köbler, X. Li, A. Abate, S. Albrecht, M. Creatore, *ACS Appl. Mater. Interfaces* **2022**, *14*, 2166.
[18] Y. Chen, Z. Yang, X. Jia, Y. Wu, N. Yuan, J. Ding, W.-H. Zhang, S. (Frank) Liu, *Nano Energy* **2019**, *61*, 148.
[19] J.-W. Liang, Y. Firdaus, R. Azmi, H. Faber, D. Kaltsas, C. H. Kang, M. I. Nugraha, E. Yengel, T. K. Ng, S. De Wolf, L. Tsetseris, B. S. Ooi, T. D. Anthopoulos, *ACS Energy Lett.* **2022**, *7*, 3139.
[20] N. Arora, M. I. Dar, A. Hinderhofer, N. Pellet, F. Schreiber, S. M. Zakeeruddin, M. Grätzel, *Science* **2017**, *358*, 768.
[21] I. S. Yang, S. Lee, J. Choi, M. T. Jung, J. Kim, W. I. Lee, *J. Mater. Chem. A* **2019**, *7*, 6028.
[22] V. E. Madhavan, I. Zimmermann, A. A. B. Baloch, A. Manekkathodi, A. Belaidi, N. Tabet, M. K. Nazeeruddin, *ACS Appl. Energy Mater.* **2020**, *3*, 114.
[23] J. Sun, N. Zhang, J. Wu, W. Yang, H. He, M. Huang, Y. Zeng, X. Yang, Z. Ying, G. Qin, C. Shou, J. Sheng, J. Ye, *ACS Appl. Mater. Interfaces* **2022**, *14*, 52223.
[24] I. S. Yang, Y. J. Park, Y. Hwang, H. C. Yang, J. Kim, W. I. Lee, *Nanomaterials* **2022**, *12*, 3969.
[25] C. Liu, L. Zhang, Y. Li, X. Zhou, S. She, X. Wang, Y. Tian, A. K. Y. Jen, B. Xu, *Advanced Functional Materials* **2020**, *30*, 1908462.
[26] A. Liu, H. Zhu, M.-G. Kim, J. Kim, Y.-Y. Noh, *Advanced Science* **2021**, *8*, 2100546.
[27] H. Wang, Z. Yu, J. Lai, X. Song, X. Yang, A. Hagfeldt, L. Sun, *J. Mater. Chem. A* **2018**, *6*, 21435.
[28] M. Huangfu, Y. Shen, G. Zhu, K. Xu, M. Cao, F. Gu, L. Wang, *Applied Surface Science* **2015**, *357*, 2234.
[29] P. Worakajit, F. Hamada, D. Sahu, P. Kidkhunthod, T. Sudyoadsuk, V. Promarak, D. J. Harding, D. M. Packwood, A. Saeki, P. Pattanasattayavong, *Advanced Functional Materials* **2020**, *30*, 2002355.
[30] P. Xu, J. Liu, J. Huang, F. Yu, C.-H. Li, Y.-X. Zheng, *New J. Chem.* **2021**, *45*, 13168.
[31] V. E. Madhavan, I. Zimmermann, C. Roldán-Carmona, G. Grancini, M. Buffiere, A. Belaidi, M. K. Nazeeruddin, *ACS Energy Lett.* **2016**, *1*, 1112.
[32] L. Mohan, S. R. Ratnasingham, J. Panidi, T. D. Anthopoulos, R. Binions, M. A. McLachlan, J. Briscoe, *Crystal Growth & Design* **2020**, *20*, 5380.
[33] S. S. Mali, J. V. Patil, C. K. Hong, *J. Mater. Chem. A* **2019**, *7*, 10246.
[34] I. Zimmermann, M. Provost, S. Mejaouri, M. Al Atem, A. Blaizot, A. Duchatelet, S. Collin, J. Rousset, *ACS Appl. Mater. Interfaces* **2022**, *14*, 11636.
[35] I. Zimmermann, M. Al Atem, O. Fournier, S. Bernard, S. Jutteau, L. Lombez, J. Rousset, *Advanced Materials Interfaces* **2021**, *8*, 2100743.

[36] H. Wang, F. Ye, J. Liang, Y. Liu, X. Hu, S. Zhou, C. Chen, W. Ke, C. Tao, G. Fang, *Joule* **2022**, *6*, 2869.
[37] H. Uchiyama, D. Shimaoka, H. Kozuka, *Soft Matter* **2012**, *8*, 11318.
[38] R. D. Deegan, O. Bakajin, T. F. Dupont, G. Huber, S. R. Nagel, T. A. Witten, *Nature* **1997**, *389*, 827.
[39] Carl Ohrenberg, Louise M. Liable-Sands, and Arnold L. Rheingold, C. G. Riordan*, *Structural Diversity in a Family of Copper(I) Thioether Complexes*, American Chemical Society, **2001**.
[40] S. G. Murray, F. R. Hartley, *Coordination chemistry of thioethers, selenoethers, and telluroethers in transition-metal complexes*, American Chemical Society, **2002**.
[41] K. M. Henline, C. Wang, R. D. Pike, J. C. Ahern, B. Sousa, H. H. Patterson, A. T. Kerr, C. L. Cahill, *Crystal Growth & Design* **2014**, *14*, 1449.
[42] G. Ayala, R. D. Pike, *Polyhedron* **2016**, *115*, 242.
[43] U. Er, K. C. Icli, M. Ozenbas, *J Solid State Electrochem* **2020**, *24*, 293.
[44] A. Delamarre, L. Lombez, J. F. Guillemoles, In *Physics, Simulation, and Photonic Engineering of Photovoltaic Devices*, SPIE, **2012**, pp. 206–213.
[45] A. Delamarre, L. Lombez, J.-F. Guillemoles, *Appl. Phys. Lett.* **2012**, *100*, 131108.
[46] J. Barichello, D. Di Girolamo, E. Nonni, B. Paci, A. Generosi, M. Kim, A. Levtchenko, S. Cacovich, A. Di Carlo, F. Matteocci, *Solar RRL* **2023**, *7*, 2200739.
[47] P. Wurfel, *J. Phys. C: Solid State Phys.* **1982**, *15*, 3967.
[48] I. L. Braly, D. W. deQuilettes, L. M. Pazos-Outón, S. Burke, M. E. Ziffer, D. S. Ginger, H. W. Hillhouse, *Nature Photon* **2018**, *12*, 355.
[49] E. T. Hoke, D. J. Slotcavage, E. R. Dohner, A. R. Bowring, H. I. Karunadasa, M. D. McGehee, *Chem. Sci.* **2015**, *6*, 613.
[50] F. Staub, H. Hempel, J.-C. Hebig, J. Mock, U. W. Paetzold, U. Rau, T. Unold, T. Kirchartz, *Phys. Rev. Appl.* **2016**, *6*, 044017.
[51] S. Cacovich, G. Vidon, M. Degani, M. Legrand, L. Gouda, J.-B. Puel, Y. Vaynzof, J.-F. Guillemoles, D. Ory, G. Grancini, *Nat Commun* **2022**, *13*, 2868.
[52] J. Haddad, B. Krogmeier, B. Klingebiel, L. Krückemeier, S. Melhem, Z. Liu, J. Hüpkes, S. Mathur, T. Kirchartz, *Advanced Materials Interfaces* **2020**, *7*, 2000366.
[53] P. Caprioglio, M. Stolterfoht, C. M. Wolff, T. Unold, B. Rech, S. Albrecht, D. Neher, *Advanced Energy Materials* **2019**, *9*, 1901631.
[54] M. A. Green, *Solar Cells* **1982**, *7*, 337.
[55] O. Breitenstein, P. Altermatt, K. Ramspeck, M. A. Green, J. Zhao, A. Schenk, In *2006 IEEE 4th World Conference on Photovoltaic Energy Conference*, **2006**, pp. 879–884.
[56] J. M. Shah, Y.-L. Li, Th. Gessmann, E. F. Schubert, *Journal of Applied Physics* **2003**, *94*, 2627.
[57] P. Calado, D. Burkitt, J. Yao, J. Troughton, T. M. Watson, M. J. Carnie, A. M. Telford, B. C. O'Regan, J. Nelson, P. R. F. Barnes, *Phys. Rev. Appl.* **2019**, *11*, 044005.
[58] T. Haeger, R. Heiderhoff, T. Riedl, *J. Mater. Chem. C* **2020**, *8*, 14289.
[59] S. Zeiske, O. J. Sandberg, N. Zarrabi, C. M. Wolff, M. Raoufi, F. Peña-Camargo, E. Gutierrez-Partida, P. Meredith, M. Stolterfoht, A. Armin, *J. Phys. Chem. Lett.* **2022**, *13*, 7280.
[60] M. Ledinsky, T. Schönfeldová, J. Holovský, E. Aydin, Z. Hájková, L. Landová, N. Neyková, A. Fejfar, S. De Wolf, *J. Phys. Chem. Lett.* **2019**, *10*, 1368.

This work highlights the deposition of copper thiocyanate (CuSCN) by slot-die coating as an inorganic hole transport layer for perovskite solar cells. Devices and mini-modules with efficiencies of 19.1% and 14.7% respectively are fabricated utilizing fully up-scalable and

industrially relevant wet deposition processes. Semi-transparent mini-modules were shown to retain more than 80% of their initial efficiency after 500h of illumination.

Iwan Zimmermann, Nao Harada, Thomas Guillemot, Celia Aider, K. M. Muhammed Salim, Van Son Nguyen, Jean Castillon, Marion Provost, Karim Medjoubi, Stefania Cacovich, Daniel Ory, Jean Rousset*

Slot-Die-Deposition of CuSCN Using Asymmetric Alkyl Sulfides as Co-Solvent for Low-Cost and Fully Scalable Perovskite Solar Sell Fabrication

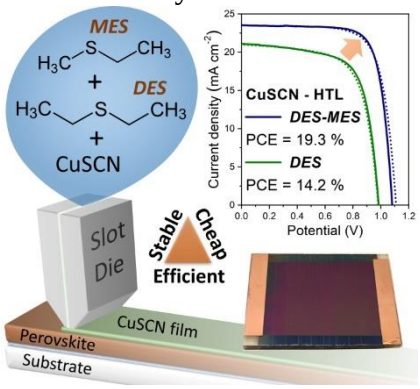

Supporting Information

Slot-Die-Deposition of CuSCN Using Asymmetric Alkyl Sulfides as Co-Solvent for Low-Cost and Fully Scalable Perovskite Solar Sell Fabrication

Iwan Zimmermann, Nao Harada, Thomas Guillemot, Celia Aider, K. M. Muhammed Salim, Van Son Nguyen, Jean Castillon, Marion Provost, Karim Medjoubi, Stefania Cacovich, Daniel Ory, Jean Rousset*

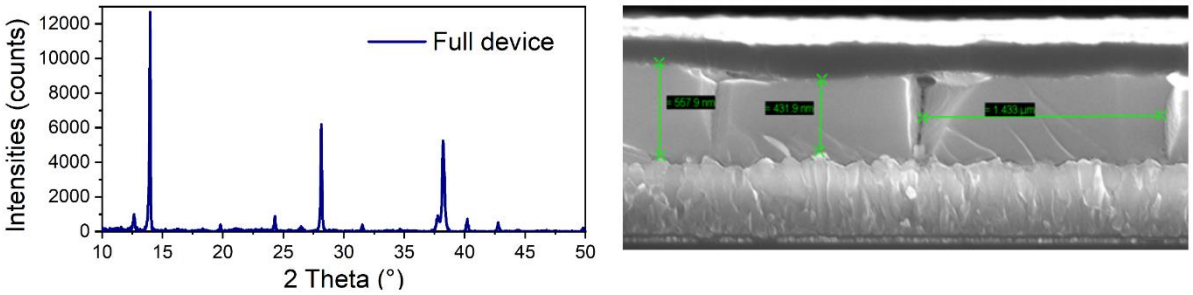

Figure S1 XRD pattern of a full device (FTO/SnO_2/perovskite/Spiro/Au) and corresponding cross sectional SEM image.

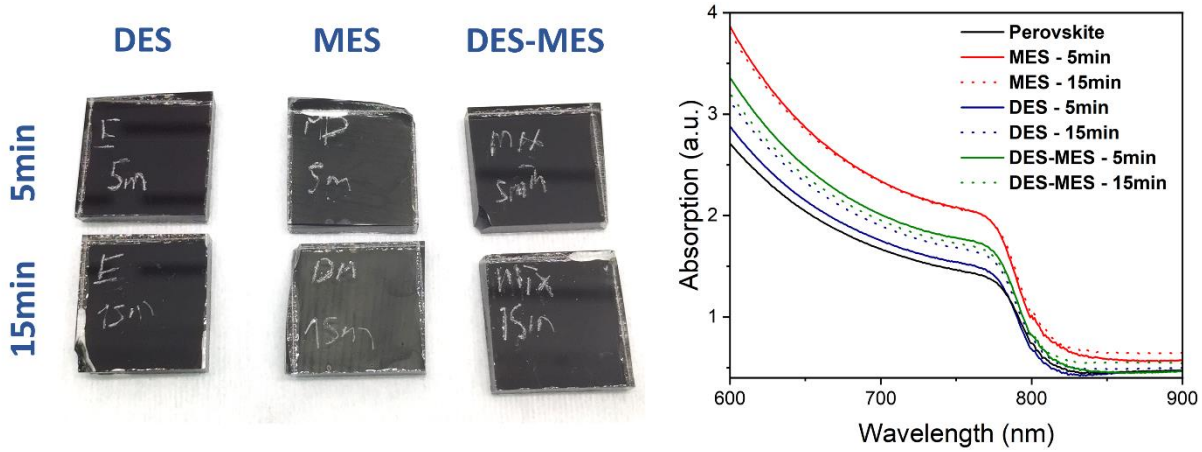

Figure S2 Pictures of perovskite films after dipping into different solvent mixtures for 5 and 15 minutes respectively. Photos taken from the glass side (left). Corresponding absorption spectra of the dipped films (right).

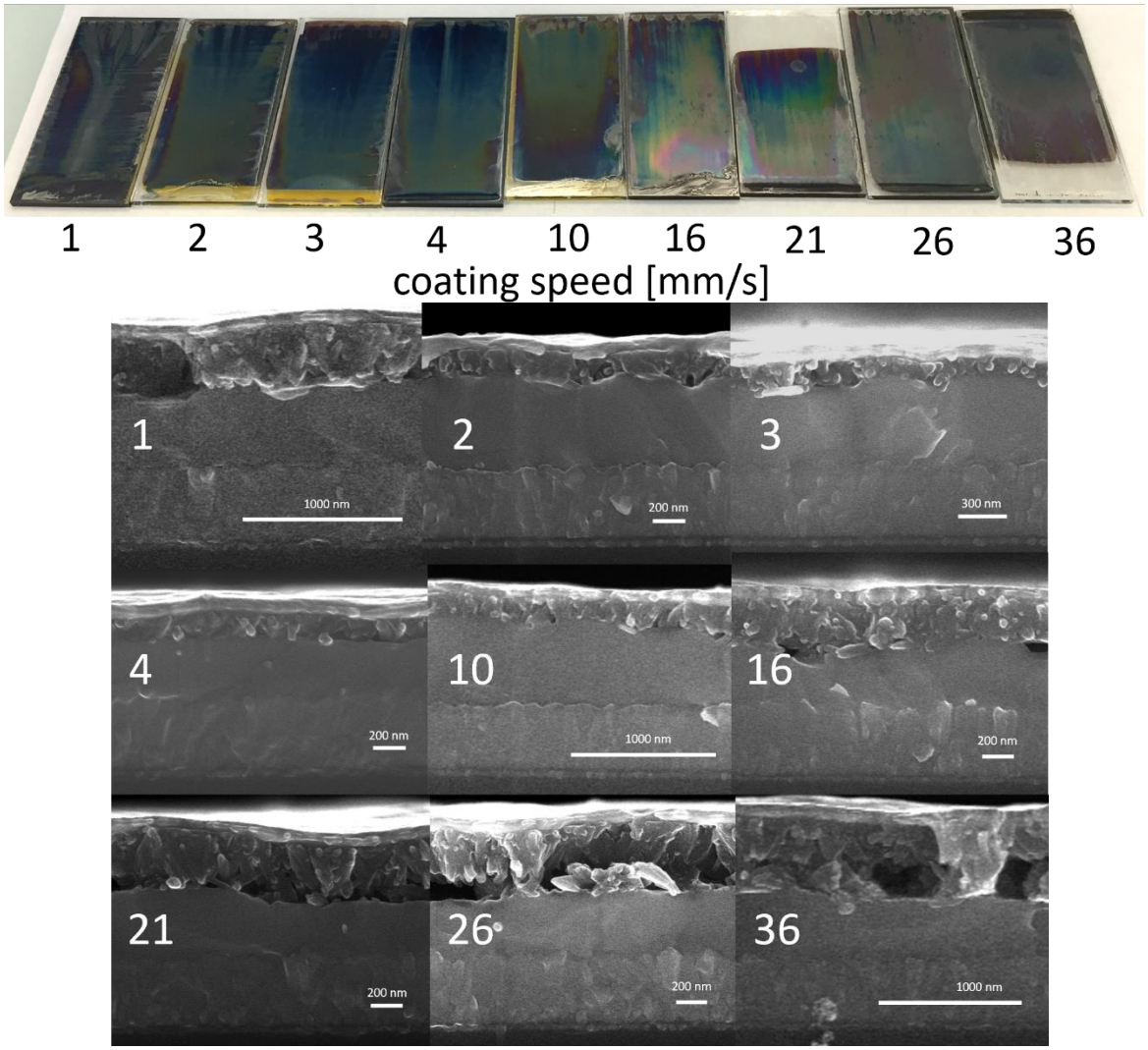

Figure S3 Images of CuSCN layers deposited onto perovskite using different coating speeds. Snapshots of the corresponding SEM cross-sectional images are shown below.

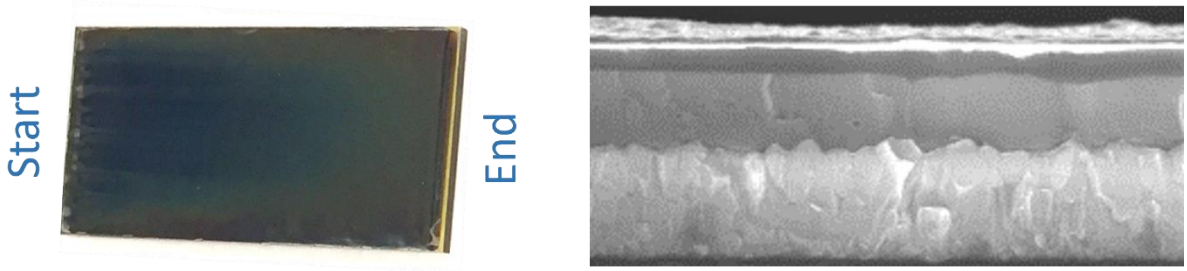

Figure S4 CuSCN film deposited onto perovskite with the optimized slot-die parameters and a corresponding SEM image. The CuSCN layer is around 100 nm thick.

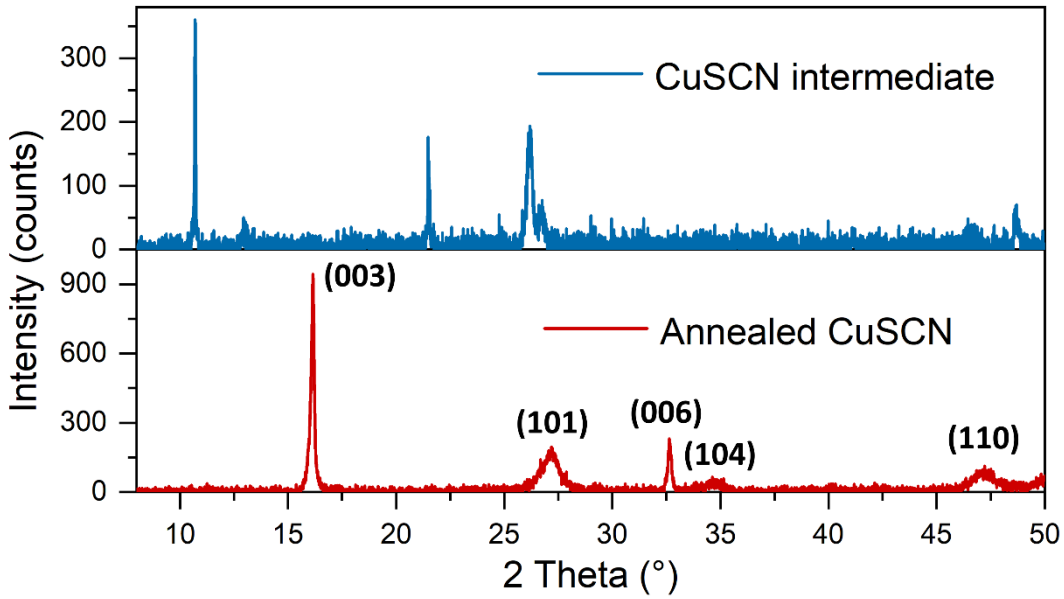

Figure S5 XRD patterns of CuSCN layers deposited onto glass using the optimized DES-MES ink. Drop-casting is used to obtain relatively thick layers necessary for a good XRD signal. The CuSCN intermediate is obtained by evaporation of the solvent at room temperature during 5min. Formation of dense beta CuSCN is observed after annealing the sample at 85°C for 10 min. CuSCN peaks are indexed according to a rhombohedral crystal system as previously reported.[43]

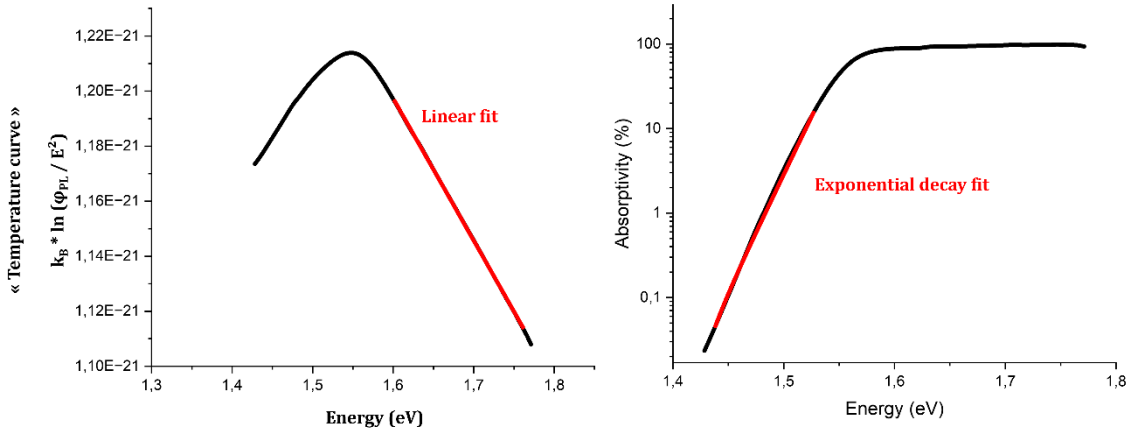

Figure S6 Parameters extracted from PL spectra. a) Temperature curve b) Absorptivity. The temperature was first extracted from the PL spectra by fitting the slope of their high-energy region. The temperature is determined by dividing the electric charge (1.6 e-19 C) by the linear fit of slope at high energy. A typical value of 305 K is obtained by this method with a good accuracy of the fit. This can be explained by a slight increase of the temperature during the hyperspectral measurement due to the LED heating up the sample. In addition, hybrid perovskites have low thermal conductivity around 0.5 $Wm^{-1}K^{-1}$ making it challenging to

effectively dissipating the heat.[58] The Urbach energy Eu was also extracted independently by fitting with a mono-exponential decay the slope (log scale) in the sub-band-gap energy range of the absorptivity curves. Typical values of 13 meV were obtain with rather good precision which is in good agreement with the literature and characteristic of a low structural disorder in the absorber.[59,60].

Name	Eg (eV)	Std (eV)	QFLS (eV)	Std (eV)
DES-MES-1	1,5502	5,32E-04	1,1012	4,70E-03
DES-MES-2	1,5513	4,40E-04	1,1044	3,80E-03
DES-MES-3	1,5501	5,35E-04	1,1052	2,90E-03
DES-MES-4	1,5514	6,06E-04	1,1042	3,00E-03
DES-MES-avg	1,5508	5,35E-04	1,1037	4,00E-03
DES-1	1,5497	0,001	1,1097	0,009
DES-2	1,5493	0,0015	1,1065	0,0101
DES-3	1,5507	0,0017	1,0919	0,0087
DES--4	1,5493	8,14E-04	1,0885	3,60E-03
DES-avg	1,5498	0,0014	1,0991	0,0123

Table S1 Eg and QFLS mean values and standard deviation for DES-MES and DES 4 samples and average of the 4.

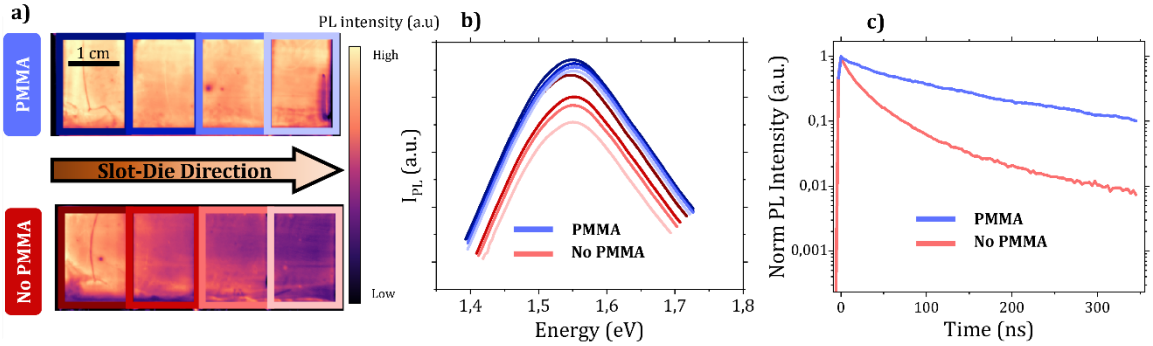

Figure S7 Effect of PMMA layer on optical properties of DES-MES sample. a) Hyperspectral image centered at 800 nm (PL peak position) for DES-MES sample with PMMA (first line) and without PMMA (second line). b) Average PL spectra of all samples. c) TRPL of samples n° 3 with and without PMMA.

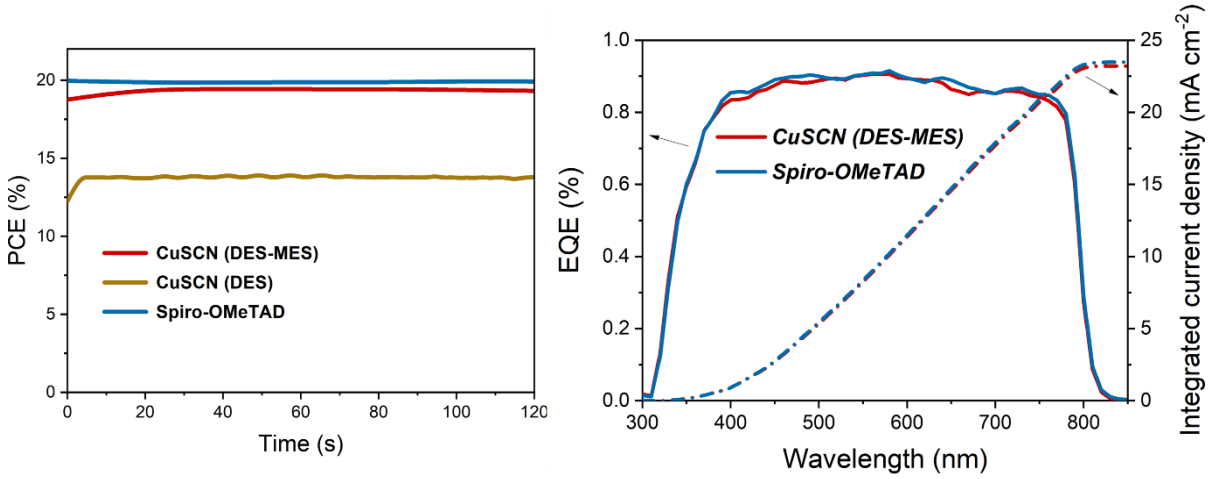

Figure S8 Stabilized power output (MPPT tracking) of the champion devices (left) and external quantum efficiency (EQE) measurements (right).

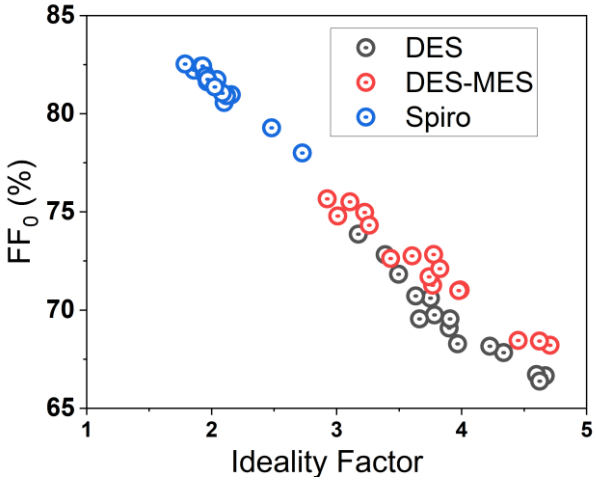

Figure S9 Parasitic resistances free Fill Factor FF_0 as a function of Ideality Factor

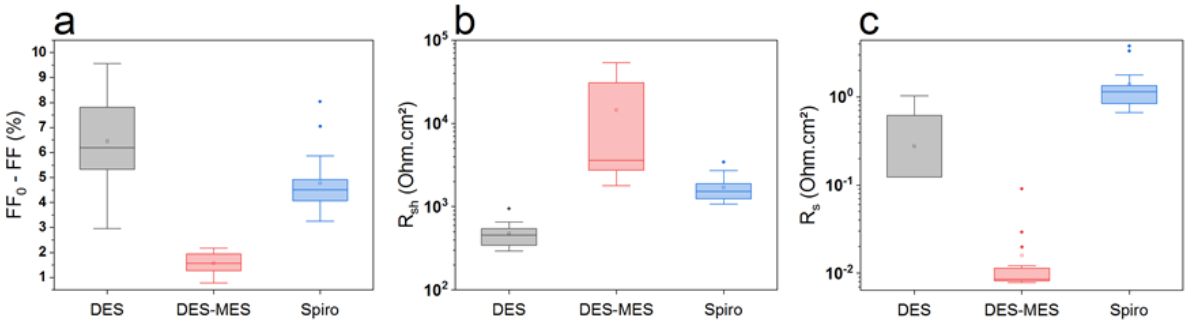

Figure S10 (a) Absolute loss in Fill Factor "FF_0-FF" due to parasitic resistances, (b) Shunt Resistance, (c) Series Resistance

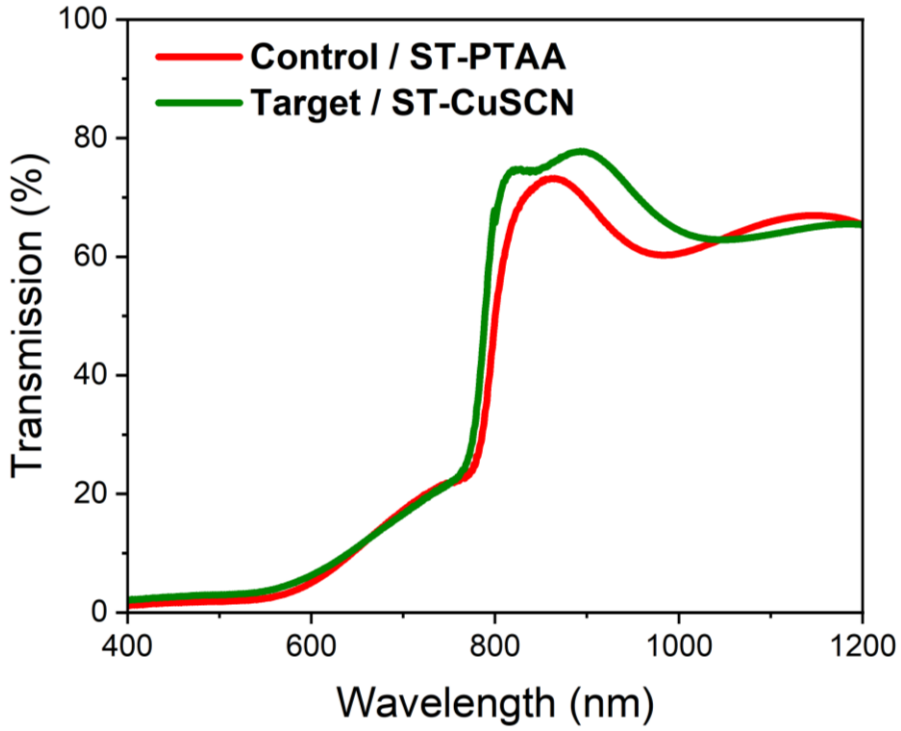

Figure S11 Transmission data of complete semi-transparent mini-modules with PTAA (red) and CuSCN (green) as hole selective layers respectively.